Research Article

Nano Research
2022, 15(3): 2674–2681

ISSN 1998-0124 CN 11-5974/O4
https://doi.org/10.1007/s12274-021-3774-4

Effects of interlayer coupling on the excitons and electronic structures of WS_2/hBN/MoS_2 van der Waals heterostructures

Xudan Zhu[1], Junbo He[1], Rongjun Zhang[1] (✉), Chunxiao Cong[2] (✉), Yuxiang Zheng[1], Hao Zhang[1], Songyou Wang[1], Haibin Zhao[1], Meiping Zhu[3], Shanwen Zhang[4], Shaojuan Li[5], and Liangyao Chen[1]

[1] *Key Laboratory of Micro and Nano Photonic Structures, Ministry of Education, Shanghai Engineering Research Center of Ultra-Precision Optical Manufacturing, School of Information Science and Engineering, Fudan University, Shanghai 200433, China*
[2] *State Key Laboratory of ASIC and System, School of Information Science and Engineering, Fudan University, Shanghai 200433, China*
[3] *Laboratory of Thin Film Optics, Shanghai Institute of Optics and Fine Mechanics, Chinese Academy of Sciences, Shanghai 201800, China*
[4] *Grating Technology Laboratory, Changchun Institute of Optics and Fine Mechanics and Physics, Chinese Academy of Sciences, Changchun 130033, China*
[5] *State Key Laboratory of Applied Optics, Changchun Institute of Optics Fine Mechanics and Physics, Chinese Academy of Sciences, Changchun 130033, China*

Received: 20 May 2021 / **Revised:** 19 July 2021 / **Accepted:** 27 July 2021

ABSTRACT

Inserting hexagonal boron nitride (hBN) as barrier layers into bilayer transition metal dichalcogenides heterointerface has been proved an efficient method to improve two dimensional tunneling optoelectronic device performance. Nevertheless, the physical picture of interlayer coupling effect during incorporation of monolayer (1L-) hBN is not explicit yet. In this article, spectroscopic ellipsometry was used to experimentally obtain the broadband excitonic and critical point properties of WS_2/MoS_2 and WS_2/hBN/MoS_2 van der Waals heterostructures. We find that 1L-hBN can only slightly block the interlayer electron transfer from WS_2 layer to MoS_2 layer. Moreover, insertion of 1L-hBN weakens the interlayer coupling effect by releasing quantum confinement and reducing efficient dielectric screening. Consequently, the exciton binding energies in WS_2/hBN/MoS_2 heterostructures blueshift comparing to those in WS_2/MoS_2 heterostructures. In this exciton binding energies tuning process, the reducing dielectric screening effect plays a leading role. In the meantime, the quasi-particle (QP) bandgap remains unchanged before and after 1L-hBN insertion, which is attributed to released quantum confinement and decreased dielectric screening effects canceling each other. Unchanged QP bandgap as along with blueshift exciton binding energies lead to the redshift exciton transition energies in WS_2/hBN/MoS_2 heterostructures.

KEYWORDS

two-dimensional (2D) van der Waals heterostructure, interlayer coupling, excitons, critical points, spectroscopic ellipsometry

1 Introduction

Two-dimensional (2D) layered transition metal dichalcogenides (TMDs), especially tungsten disulfide (WS_2) and molybdenum disulfide (MoS_2) have become fundamental building blocks in artificially engineered next generation nano-optoelectronic devices [1–4]. It is due to their unique appreciable and tunable bandgaps (1.0–2.1 eV), spin valley polarization, and strong exciton effects [5, 6].

Vertical TMDs van der Waals heterostructures (vdWHs) are reassembled by 2D-TMDs without lattice matching requirement, which have extensive applications such as light emitting diodes [7, 8], field-effect transistors [9–11], sensors [3, 12–14], sodium ion batteries [15], photocatalytic devices [16–18], solar cells [19], quantum communication devices [20]. However, the external quantum efficiency (EQE) for 2D-light emitting diodes (2D-LEDs), as well as the responsivity for 2D-photodetectors are still relatively poor, which has been mainly blamed on the large dark current [1]. In order to dampen dark current, researchers inserted hexagonal boron nitride (hBN) (2D-insulators) into the interface of vdWHs as tunneling barrier layers [20–22], which has been proved an efficient way improving device performance [23].

Nonetheless, the fundamental physical mechanism of hBN insertion introducing interlayer coupling effect is not clear yet. As for 2D vdWHs, whose optical properties are strongly influenced by interlayer coupling effects [21, 24–27]. In terms of optical behavior of vdWHs, it is determined by electronic structures and exciton properties, as a consequence of the weak screening of electron-hole interaction [28–30]. Thereout, it is of great significance to study the tuned interlayer coupling effects on the exciton properties and electronic structures after the insertion of hBN.

Although, some first-principle calculating and experimental researches addressing the role of 1L-hBN barrier layer in TMDs vdWHs have been reported, a certain extent, there exists contradictions in the conclusions they have reached [21, 31, 32].

Address correspondence to Rongjun Zhang, rjzhang@fudan.edu.cn; Chunxiao Cong, cxcong@fudan.edu.cn

In 2017, Simone Latini et al. reported a first-principle study on MoS_2/hBN/WSe_2 vdWHs [31], predicting that after intercalation of 1L-hBN, the exciton binding energies significantly redshift, on contrast, the quasi-particle (QP) band gap renormalization is unnoticeable. Moreover, the binding energy of interlayer exciton redshifts, on contrast, intralayer exciton binding energies will blueshift. While, an experimental study on WSe_2/hBN/MoS_2 vdWHs [21] reported that 1L-hBN insertion will not fully suppress the interlayer interaction in vdWHs, but three hBN layers could. However, another photoluminescence (PL) study on $MoSe_2$/hBN/WSe_2 vdWHs [32] found that the 2D heterostructure system behaves as isolated monolayers after inserting 1L-hBN. Under this circumstance, 1L-hBN seems strong enough to cut off the interlayer interaction between two TMDs layers. Thus, a detailed experimental investigation on interlayer coupling effects on electronic structures and exciton properties is crucial for the development of potential optical applications in electronic and optoelectronic devices with likewise tunneling layers inserted heterostructures.

Additionally, interlayer coupling effects include four major factors: crystal lattice twisting angle, interlayer distance, quantum confinement effect, and dielectric screening effect. Comprehensive analysis of these factors while 1L-hBN insertion is required. Researchers implemented their experimental studies on electronic structures of 2D materials by angle-resolved photoemission spectroscopy (ARPES) and scanning tunneling spectroscopy (STS). However, ARPES analysis of exfoliated small materials is lacking of the energy resolution needed to measure such quantities as band offsets and hybridization shifts [33]. As for STS, it can only obtain the QP bandgap at band edge, but loose electronic structure details in deeper valence band or in higher conduction band [34]. In terms of the excitons, optical reflection spectroscopy and PL are most commonly used experimental technologies. Although, using optical reflection spectroscopy, beside the ground states, the full sequence of excited exciton states of excitons can be obtained, the excited exciton states have relatively low spectral weight [35]. This means that these excited states are usually not be focused for applications. Moreover, PL spectra can only obtain the optical bandgap related information, which includes only the first few low energy exciton peaks. Specially, spectroscopic ellipsometry (SE) has proven effective for accessing the broadband optical properties of the thin films in a sensitive, precise, and nondestructive fashion [36, 37]. Thereout, SE is well suited to investigate the optical properties of 2D materials and their vdWHs [29, 38, 39].

In this work, SE was employed to study the interlayer coupling effect on the broadband excitonic and critical point (CP) properties of WS_2/hBN/MoS_2 vdWHs experimentally and systematically. And supplemented by Raman and PL spectroscopy measurements. Here, the transition energies of the CPs (with photon energy range from 1.5 to 6.5 eV) in WS_2/hBN/MoS_2 and WS_2/MoS_2 vdWHs are determined using the second derivative of the dielectric function, $d^2\varepsilon(E)/dE^2$, which is the standard critical point (SCP) model. We must stress that the CPs are corresponding to the interband direct transitions. Then the transition energies of CPs equal to interband energy difference in the Brillouin zone (BZ). Through comparing the CP transition energies of two vdWHs, how the changing interlayer coupling effect affects the electronic structures of the vdWHs was studied. Moreover, the discrete states of the excitons can be modeled by a broadened Lorentzian line shape, from which the binding energies and transition energies of the excitons in WS_2/MoS_2 and WS_2/hBN/MoS_2 vdWHs were obtained. And the aforementioned factors of interlayer coupling effect were discussed in detail separately. Our results provide a distinct physical picture of interlayer coupling effects on optical properties of WS_2/hBN/MoS_2 vdWHs, which is expected be generalized to analogous TMDs vdWHs. This could benefit the new optoelectronic device design and device performance improvement.

2 Results and discussion

2.1 Heterostructure preparation

Centimeter-area 1L-WS_2, 1L-MoS_2, and 1L-hBN films were fabricated by chemical vapor deposition (CVD) on Si/SiO_2 substrates separately. Then, the 1L-films have been physically transferred and stacked to the c-plane (0001) sapphire substrates in sequence as vertical WS_2/MoS_2 and WS_2/hBN/MoS_2 vdWHs, and each transfer process was followed with a same annealing process. After the annealing treatment, the contaminants (trapped adsorbates) at interfaces in vdWHs will be efficiently removed, which makes the component layers combine more tightly and largely improves the exciton effects [24]. This guarantees the interlayer coupling in vdWHs will not be weakened due to the transfer process. Moreover, what must be stressed, the c-plane (0001) sapphire crystals are widely used as substrates for 2D semiconductors, especially TMDs thin films [40]. Due to their slight optical anisotropy in the visible–ultraviolet region [41], our spectral range (1.2–6.5 eV) is included. This guarantees the feasibility treating the c-plane (0001) sapphire substrates as isotropic. The detailed 1L-TMDs film synthesis and transfer method have been reported elsewhere [29, 39, 42]. Figure 1(a) shows a schematic view of the vertically stacked WS_2/hBN/MoS_2 vdWH. 1L-hBN has been sandwiched by 1L-MoS_2 layer (top) and 1L-WS_2 layer (bottom). Unlike normal bilayer TMDs vdWHs, taking the barrier heights at each side of the hBN interface into account, with reference to the previous reported electron and hole barrier heights between MoS_2 and hBN interfaces [43], the band alignment of WS_2/hBN/MoS_2 vdWH was schematically illustrated in Fig. 1(b). The WS_2/MoS_2 vdWH is of type-II band alignment, in which electrons and holes are inclined to transfer across the interface between two TMDs layers [29]. However, owning to the barriers, the originally spontaneous transfer of the electrons from WS_2 to MoS_2 (holes move reversely) is impeded. Fewer charges transfer across the interface tunneling barriers and bond as interlayer excitons. Comparing with the interlayer excitons in WS_2/MoS_2 vdWHs, those in WS_2/hBN/MoS_2 have longer lifetime. By locking the interlayer charge transfer, longer exciton lifetime is obtained. Then the dark current of tunneling devices is reduced efficiently [1].

2.2 Raman features

Figure 1(c) shows the Raman spectra of 1L-MoS_2, 1L-WS_2, WS_2/MoS_2, WS_2/hBN/MoS_2 vdWHs excited with a 532 nm laser at room temperature. Only the typical modes E_{2g}^1 (in-plane vibration) and A_{1g} (out-of-plane vibration) of the samples are displayed for comparation. Notably, according to lattice symmetry analysis [44], the precise notation of Raman modes in 1L-WS_2, 1L-MoS_2 and those of counterparts in TMDs vdWHs should be different. For simplification, the same notations of E_{2g}^1 and A_{1g} were used for 1L-TMDs and the corresponding TMDs vdWHs here. The Raman modes in our 1L-TMDs samples consistent with previous reports [29, 45]. The frequency difference of these two Raman modes gives precise identification of monolayer structures of the MoS_2 and WS_2 films. And the Raman signal of 1L-hBN is shown in the Fig. S1 in the Electronic Supplementary Material (ESM), which declares its monolayer structure.

Furthermore, E_{2g}^1 modes in WS_2/MoS_2 vdWHs show a significant redshift compared with the counterparts in the

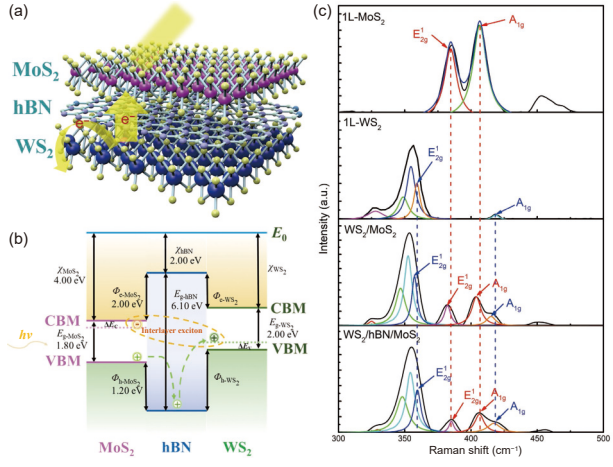

Figure 1 (a) Schematic of the WS_2/hBN/MoS_2 vertical heterostructure, where centimeter-scale 1L-MoS_2 and 1L-WS_2, and 1L-hBN fully covers the sapphire substrates, and (b) energy band diagrams of WS_2/hBN/MoS_2 heterostructure shown at flat band model (χ, electron affinity; E_g, bandgap; Φ_e, electron tunneling barrier; Φ_h, hole tunneling barrier; CBM, conduction band minimum; VBM, valence band maximum). The data of χ_{hBN}, Φ_{e-MoS_2}, and Φ_{h-MoS_2} are from previous report [43]. (c) Raman spectra of the 1L-MoS_2, 1L-WS_2, WS_2/MoS_2, and WS_2/hBN/MoS_2 films obtained under 532 nm laser excitation at room temperature. Only the typical peaks of MoS_2 (labeled by red font color) and WS_2 (labeled by blue font color) were displayed for comparison, and the detailed multiple peaks were obtained by Lorentz fitting. The dashed lines are the guides to the eye.

corresponding IL-TMDs samples. Since the E_{2g}^1 mode is sensitive to build-in strain, we can attribute this to the lattice mismatch between MoS_2 and WS_2 layer, which enhances the overall restoring forces on the atoms [24, 45, 46]. Besides, the A_{1g} peaks in 1L-TMDs redshift in WS_2/MoS_2 vdWH. This indicates the spontaneous interlayer charge transfer from WS_2 to MoS_2 (depicted in Fig. 1(b)). These phenomena suggest the strong interlayer coupling in the WS_2/MoS_2 vdWH, and strong evidence that WS_2 and MoS_2 interact well with each other in WS_2/MoS_2 vdWH [24]. Moreover, it is observed that the redshifts of two Raman peaks are largely reduced in MoS_2/hBN/WS_2 vdWH, compared with the peak shift in the MoS_2/WS_2 vdWH. Especially, the E_{2g}^1 modes of MoS_2 and WS_2 in MoS_2/hBN/WS_2 vdWH almost the same as their corresponding Raman peaks in the monolayer samples. The presence of the Raman bands homing expression indicates that the build-in strain is released, to a large extent, by inserting 1L-hBN layer into MoS_2/WS_2 vdWH. However, the A_{1g} modes still show a slight redshift in MoS_2/hBN/WS_2 vdWH. This suggests that despite the barrier heights introduced by 1L-hBN block the charge transfer at interface, there still are residual interlayer charge transfer from WS_2 to MoS_2 in MoS_2/hBN/WS_2 vdWH. Therefore, Raman results show that 1L-hBN will not completely inhibit interlayer interaction between two TMDs layers.

2.3 PL signals

PL characteristics of vdWHs are expected to depend on the degree of interlayer coupling strength [27]. PL spectroscopy is employed to probe the charge transfer across the 2D heterojunctions and exciton properties. The PL spectra of the vdWHs are excited with a 532 nm laser at different temperature (100, 200, and 300 K) and locations (5 random locations over the whole film surface) shown as Fig. S2 in the ESM. The location dependent PL spectra (Figs. S2(a) and S2(b) in the ESM) showed minor PL intensity differences, declaring our vdWHs are uniform almost over whole area. Relatively, the PL results of most tight binding location (location 3 for all vdWH samples) were chosen for comparation shown as Figs. 2(c) and 2(d), which could minimize experimental errors. In the meantime, the low-temperature PL spectra (100 K and 200 K) of vdWH samples (Figs. S2(c) and S2(d) in the ESM) also exhibit six characteristic peaks as room temperature PL spectra (Figs. 2(c) and 2(d)). The PL peaks can be distinguished which based on the peak position shift trend with changing temperature. In addition, the PL signals of the sapphire substrates of 1L-TMDs films have been deducted before analysis. While the

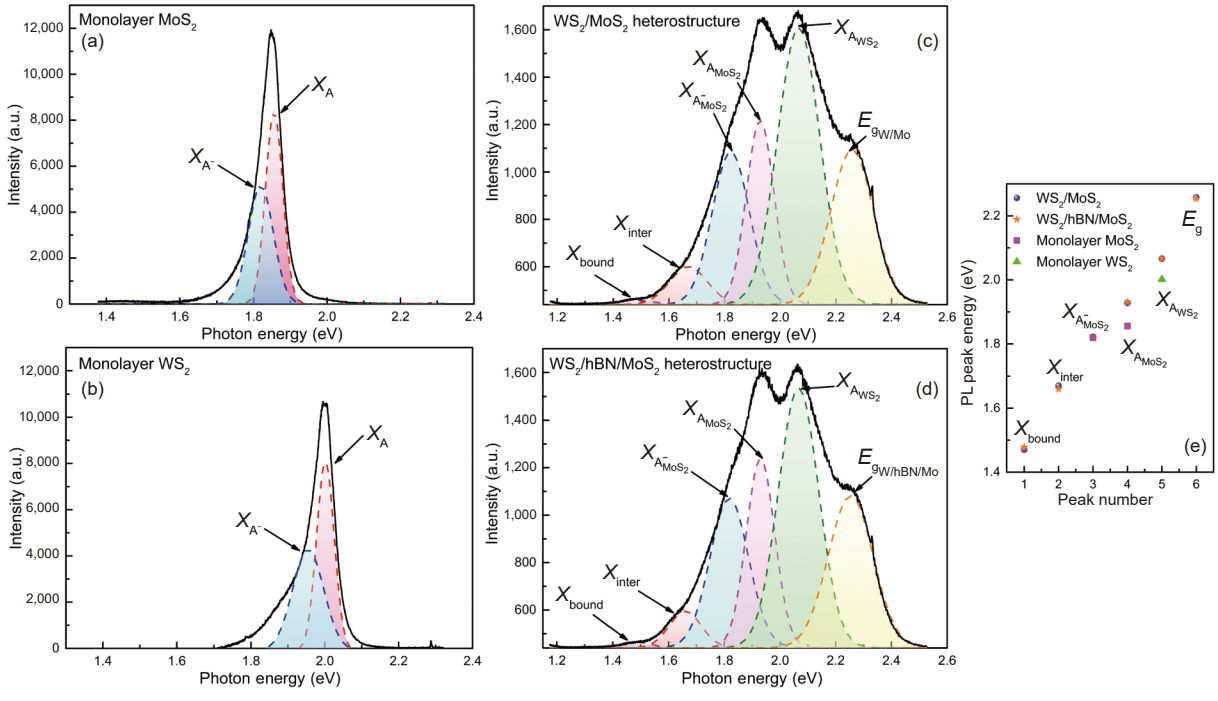

Figure 2 The PL spectra of the (a) 1L-MoS_2, (b) 1L-WS_2, (c) WS_2/MoS_2 and (d) WS_2/hBN/MoS_2 films excited by 532 nm laser at room temperature. By fitting the PL spectra via multiple Guassian functions, the detailed multiple exciton peaks were obtained. The notation of X_{bound}, X_{inter}, X_{A-}, X_A, and E_g were used indicating PL peaks of bound exciton, interlayer exciton, trion, A neutral exciton, indirect energy gap, respectively, which were expressed as dash lines filled with different color. (e) The PL peak energies of four samples. The purple spot, orange star, pink square, green triangle symbols represent PL peaks in WS_2/MoS_2, WS_2/hBN/MoS_2, 1L-MoS_2, and 1L-WS_2 samples, respectively.

sapphire substrate PL signals were weak in vdWHs samples, which attributed to thicker heterostructures.

As shown in Figs. 2(a) and 2(b), the emission energies of trion and neutral A exciton in 1L-MoS_2 (1L-WS_2) are located at 1.820 eV (1.955 eV) and 1.855 eV (2.002 eV), respectively, which are consistent with previously reported values [29, 47]. And the energy difference of these two peaks is the binding energies of trions (E_{bA^-}) [48], which are 36.2 meV in 1L-MoS_2 ($E_{bA^-\,MoS_2}$) and 46.6 meV in 1L-WS_2 ($E_{bA^-\,WS_2}$), respectively. Furthermore, the PL spectra acquired from the WS_2/MoS_2 vdWH (Fig. 2(c)) can be decomposed into six prominent peaks: 1.470, 1.670, 1.822, 1.928, 2.066, and 2.258 eV, respectively. With increasing photon energies, these PL peaks can be assigned to bound exciton (X_{bound}), interlayer exciton (X_{inter}), trion in top MoS_2 layer ($X_{A^-\,MoS_2}$), neutral A exciton in MoS_2 (X_{AMoS_2}), neutral A exciton in WS_2 (X_{AWS_2}), indirect bandgap of WS_2/MoS_2 ($E_{gMo/W}$), respectively. Likewise, the PL peaks of excitons and indirect bandgap of WS_2/hBN/MoS_2 vdWH have been obtained, which are 1.478 eV (X_{bound}), 1.660 eV (X_{inter}), 1.818 eV ($X_{A^-\,MoS_2}$), 1.930 eV (X_{AMoS_2}), 2.067 eV (X_{AWS_2}), and 2.254 eV ($E_{gMo/hBN/W}$), respectively.

The bound excitons in vdWHs are excitons which localize at neutral impurities or inhomogeneities [47, 49, 50]. They are likely introduced during synthesis processing and are not the focus of this paper. And according to previous theoretical calculation researches, WS_2/MoS_2 vdWHs have indirect bandgap at around 2.26 eV [28, 51]. Moreover, the corresponding absorption has been found in previous experimental studies [52, 53], and the little energy difference between absorption and emission can be blamed to stokes shift. As revealed in Figs. 2(d) and 2(e), the indirect band gap of WS_2/hBN/MoS_2 vdWHs is 2.254 eV basically equals to that of WS_2/MoS_2 vdWHs. That is to say, the large energy gap of hBN will not influence the band gap energy of WS_2/hBN/MoS_2 vdWHs.

The $E_{bA^-\,MoS_2}$ of WS_2/MoS_2 and WS_2/hBN/MoS_2 vdWHs are 106 meV and 112 meV, respectively. First, the $E_{bA^-\,MoS_2}$ of 1L-MoS_2 was compared with those of vdWHs. $E_{bA^-\,MoS_2}$ of vdWHs are significantly larger than that of 1L-MoS_2 (36.2 meV). This may be caused by electron doping in MoS_2 layer (electrons transfer from WS_2 layer) [48, 54, 55]. Contrarily, the efficient dielectric screening in vdWHs increases comparing with that in 1L-MoS_2 [29], which would redshift the trion binding energy [56]. In this case, the trion binding energies of MoS_2 layer in vdWHs are mainly depended on the electron doping effect. Next, we assumed that 1L-hBN significantly suppressed the charge transfer across the interfaces in WS_2/hBN/MoS_2 vdWHs. Then, the $E_{bA^-\,MoS_2}$ of the WS_2/hBN/MoS_2 vdWH must be smaller than that of WS_2/MoS_2 vdWHs. On the contrary, comparing the $E_{bA^-\,MoS_2}$ of two vdWHs, it can be found that inserting 1L-hBN in WS_2/MoS_2 vdWHs blueshifts the $E_{bA^-\,MoS_2}$. This clarifies that 1L-hBN cannot inhibit interlayer charge transfer in vdWHs, which is consist with our Raman results. Since the efficient dielectric constant of 1L-hBN (2.31) approximately equals to SiO_2 [57, 58], which is smaller than 1L-MoS_2 (6.3), 1L-WS_2 (6.0) and WS_2/MoS_2 vdWHs (6.5) [25, 59]. Thus, the blueshift of $E_{bA^-\,MoS_2}$ in MoS_2/hBN/WS_2 vdWH may be attributed to reduced dielectric screening.

Besides, as expected, PL quenching has been found in PL spectra of all the vdWHs (shown in Figs. 2(c) and 2(d)). This has been attributed to the interlayer charge transfer between layers owning to the type-II band alignment in WS_2/MoS_2 and WS_2/hBN/MoS_2 vdWHs (Fig. 1(b)) [29, 47]. By contrast, PL quenching effect has not been obviously further weakened in WS_2/hBN/MoS_2 vdWH, implying that the barrier heights induced by 1L-hBN are insufficient for suppressing the interlayer charge transfer. And as a consequence of charge transfer and increasing dielectric screening in vdWHs, the neutral A excitons in corresponding TMDs layers (X_{AMoS_2} and X_{AWS_2}) shifted comparing with those in isolated 1L-MoS_2 and 1L-WS_2 films [47]. Furthermore, we found that the PL peak energies of WS_2/MoS_2 vdWHs barely did not shift after inserting 1L-hBN (Fig. 2(e)), which is also strongly evident that the weak inhibition effect of interlayer charge transfer of 1L-hBN. This is in agreement with a previous PL research on MoS_2/WSe_2 vdWH [21].

2.4 Broadband electronic structures and exciton properties

The broadband (photon energy range within 1.2–6.5 eV) electronic structures and exciton properties of the vdWHs were explored by SE (detailed fitting procedures are introduced in the ESM). Additionally, as for three-layer heterostructure films, their thicknesses are only few nanometers. It is presumed that the films are optically uniaxial with differ between out-of-plane dielectric function component and the in-plane component. SE is known to be insensitive to the out-of-plane component, and its ellipsometric response is determined by the in-plane component [60]. Thus, our complex dielectric functions of the samples are pseudodielectric functions representing the in-plane component. Nonetheless, owning to the three-atom structure of 1L-WS_2 and 1L-MoS_2 in the out-of-plane direction, their out-of-plane dielectric characteristics are arguably similar to the in-plane component. Hence, SE is still powerful tool to study optical properties of 2D ultra-thin films [61]. It is worth noting that the strength of an allowed optical transitions between conduction and valence bands is proportional to the joint density of states (JDOS). And the density of the states (DOS) of electron and phonon bands possesses singularities at points where $|\nabla_k (E)|$ vanishes [62]. These points are known as CPs. The CPs are expected to occur in the BZ, where the slopes of the valence and conduction bands are horizontal or parallel [29]. The CP transition energies of vdWHs samples were obtained using SCP model. And the entire fitting parameters are listed in Table S1 in the ESM.

As revealed in Fig. 3(b), the CPs in WS_2/hBN/MoS_2 vdWHs are in accordance with those in the WS_2/MoS_2 vdWHs film near the band edge. While, relatively distinct transition energy differences appeared in higher photon energy range, where close to 1L-hBN intrinsic bandgap (~ 6.2 eV). The unchanged CP transition energies around the band edge implies that inserting 1L-hBN into WS_2/MoS_2 vdWHs has little effect on the QP bandgap, which is in great agreement with previous calculation results on MoS_2/hBN/WSe_2 vdWHs QP bandgap [31]. And the unchanged indirect energy gaps of two vdWHs have been also found in aforementioned PL results (Figs. 2(c)–2(e)). As reported in previous first-principle studies [63], in spite of the relatively interlayer weak van der Waals coupling in vdWHs, the strong out-of-plane hybridization only affects higher conduction and deeper valence regions in the electronic structure. Besides, the bandgap of 1L-hBN in our work is 6.2 eV (reveled by complex refractive index, dielectric function, and absorption coefficient spectra of 1L-hBN introduced in the ESM), which is far from the bandgap of 1L-TMDs. Hence, the electronic structure of WS_2/hBN/MoS_2 vdWHs around Femi level (E_F) is essentially a superposition of the 1L-WS_2 and 1L-MoS_2 individual contributions, which leads to the similar band edge as WS_2/MoS_2 vdWHs.

Then the exciton properties in vdWHs were studied by fitting the absorption coefficient spectra using broadened Lorentzian line shape [29, 39]. The fitting details are included in the ESM. And the fitting parameters are listed in Table S2 in the ESM. Figure 3(a) illustrates the relationship between the QP bandgap (CP transition energies, E_{th}), exciton binding energies (E_b), and the exciton transition energies (E_0), which can be expressed as $E_{th} = E_b + E_0$. As revealed in Figs. 3(c) and 3(d), after inserted with 1L-hBN, the

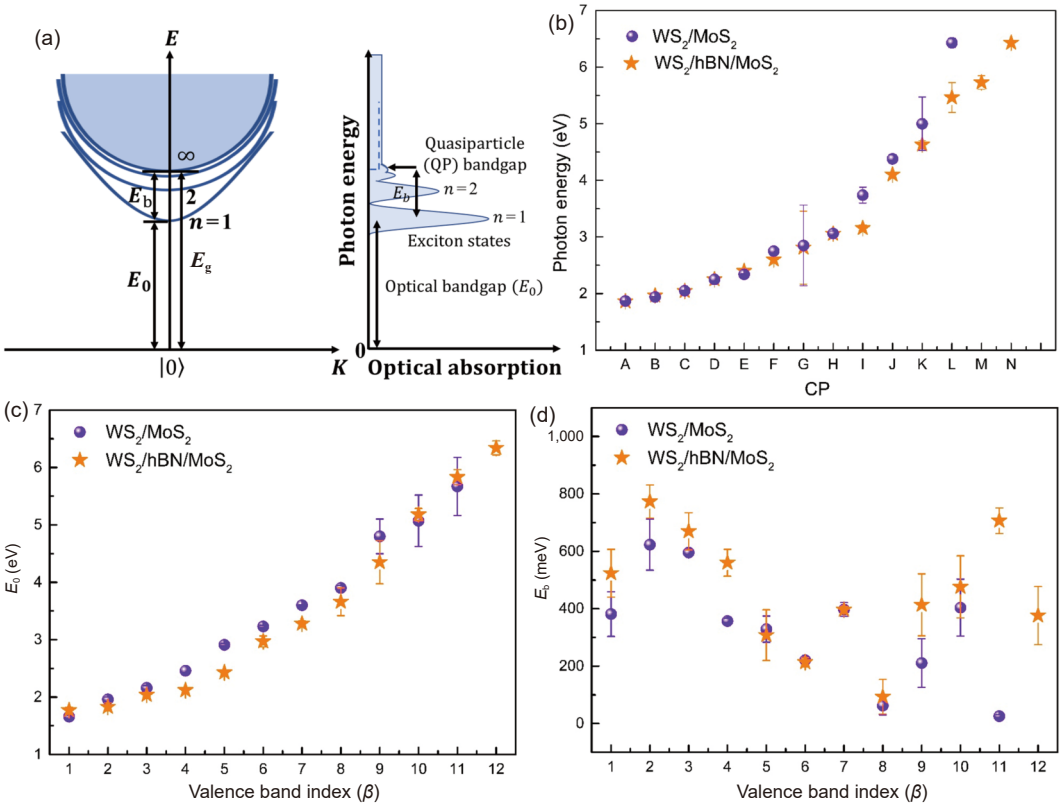

Figure 3 (a) Left panel shows the energy states of an exciton showing both its bound states n = 1 to 3 and the continuum states. E_g is the quasiparticle (QP) bandgap, E_b the exciton binding energy, and E_0 the exciton transition energy. And right panel depicts the corresponding optical absorption of the bound and continuum states. (b) CP transition energies obtained by SCP model fitting. The specific data are listed in Table S1 in the ESM. (c) Exciton transition energies and (d) exciton binding energies fitted by broaden Lorentz Line shape model. The detailed fitting results are listed in Table S2 in the ESM.

E_0 slightly redshift while E_b blueshift in WS_2/hBN/MoS_2 vdWHs comparing with those of WS_2/MoS_2 vdWHs. Firstly, considering the stable QP bandgap as observed in Fig. 3(b), the variation tendency of E_b and E_0 is self-consistent. Then, the interlayer coupling effects on exciton properties will be discussed in detail as following.

First, it has been investigated in previous studies that interfacial twists might control the local bandgap by creating an internal stacking translation [64, 65]. However, this twist-angle-dependent property has not been found in all vdWHs [26]. It has been demonstrated that the $MoSe_2$/hBN/MoS_2 vdWHs presented any twist-angle dependence [32], where the 1L-hBN is sandwiched by 1L-$MoSe_2$ and 1L-WSe_2. As introduced, this is resulted from the 1L-hBN reducing the interlayer coupling. It can be inferred that the changes of the electronic band structure and exciton properties of WS_2/hBN/MoS_2 vdWHs in our work were basically not induced from the twist angle of 1L-hBN.

Additionally, interlayer distance also plays an important role in determining strength of interlayer coupling [26, 27]. In terms of inserting 1L-hBN layer, the interlayer distance is increased. As reported by experimental [66] and calculating [31] studies, with increased interlayer distance, the interlayer coupling energy at heterointerface has been decreased and the efficient dielectric screening effect would be reduced either. This will result in the redshift of interlayer exciton E_b, while blueshift of intralayer exciton E_b in vdWHs, respectively [31]. However, this different shift trends of interlayer and intralayer excitons were not be found in our WS_2/hBN/MoS_2 vdWHs. Then, it can be concluded that the changed interlayer distance introduced by 1L-hBN is relatively weak to influence the electronic structure or exciton behavior.

Besides, it has been experimentally studied in previous researches [39, 42, 67], the quantum confinement effect is another crucial factor which will significantly tune the band structure and modulate the exciton properties, especially when the layer number of 2D material is less than four. After the insertion of 1L-hBN between the 1L-WS_2 and 1L-MoS_2 layers, the quantum confinement will be released. Consequently, the QP bandgap and exciton binding energies will redshift. Moreover, quantum confinement effect on QP bandgap was found even more remarkable. Nevertheless, the redshift of exciton binding energies (E_b) was not found in our results (Fig. 3(d)). It was observed that during the incorporation of 1L-hBN into heterointerface, the quantum confinement plays a minor role in regulating exciton binding energies. This phenomenon that un-conspicuous influence of geometric confinement effect on exciton physics has also been revealed by previous calculation study on excitons in 2D and three-dimensional (3D) layered materials [58].

Since the exciton binding energies and the QP bandgap are sensitive to dielectric screening from the immediate environment [29, 58, 68]. As aforementioned, the efficient dielectric constants of 1L-hBN, 1L-WS_2, 1L-MoS_2, and WS_2/MoS_2 vdWHs are 2.31 [57, 58], 6.0, 6.3, and 6.5 [25, 59], respectively. It can be suggested naturally that the efficient dielectric screening effect was reduced in WS_2/hBN/MoS_2 vdWHs owing to incorporation of 1L-hBN into heterointerface. According to previous investigation on dielectric screening effect on electronic band structures and excitons in vdWHs [29], decreased efficient dielectric screening leads to blueshift of QP bandgap, exciton transition energies, and exciton binding energies. As expected, the blueshift of exciton binding energies has been found in Fig. 3(d). Due to the stable electronic structure around band edge, the increasing exciton binding energies in WS_2/hBN/MoS_2 vdWHs will result in a redshift of exciton transition energies (shown in Fig. 3(c)). It also declares that the dielectric screening effect modulates the exciton transition energies by controlling their binding energies and corresponding electronic structures.

To sum up, the incorporation of 1L-hBN into WS_2/MoS_2 heterointerface reduces the strength of interlayer coupling in WS_2/hBN/MoS_2 vdWHs, where the dielectric screening effect plays a crucial role in tuning the exciton bind energies. In terms of the stable QP bandgap found in this work (Fig. 3(b)), the dielectric screening effect and quantum confinement effect must be combined for consideration. The effects of released quantum confinement and reduced efficient dielectric screening introduced by insertion of 1L-hBN cancelled out with each other. Consequently, the unchanged CP transition energies in WS_2/hBN/MoS_2 vdWHs have been found.

3 Conclusions

In this work, the interlayer coupling effects on the excitons and electronic structures of WS_2/hBN/MoS_2 vdWHs were experimentally investigated. From the results of Raman and PL spectra, it can be clarified that the weak inhibition effect of 1L-hBN on interlayer charge transfer. The barrier heights at heterointerfaces introduced by 1L-hBN can only slightly block electron transferring from 1L-WS_2 to 1L-MoS_2. Consequently, the binding energies of intralayer trions in MoS_2 layer in vdWHs (106 meV in WS_2/MoS_2 and 112 meV in WS_2/hBN/MoS_2) are all larger than that of individual 1L-MoS_2 film (36.2 meV). Moreover, the blueshift of intralayer trion binding energy in MoS_2 layer in WS_2/hBN/MoS_2 vdWHs compared to that in WS_2/MoS_2 vdWHs is caused by decreased dielectric screening effect induced by 1L-hBN insertion. Due to the reduced interlayer coupling strength after incorporation of 1L-hBN into heterointerface, the exciton binding energies in WS_2/hBN/MoS_2 vdWHs blueshift, where the dielectric screening effect plays a leading role. Furthermore, with the stable QP bandgap revealed by unchanged CP transition energies, the blueshift exciton binding energies leads to the redshift of exciton transition energies in WS_2/hBN/MoS_2 vdWHs. And the stable QP bandgap before and after the insertion of 1L-hBN is the result of the released quantum confinement and decreased dielectric screening effect canceling each other. Our results thus establish a physical picture for the influence of interlayer coupling effect on excitonic properties and electronic structures of van der Waals heterostructures, necessary for both design and performance improvement of optoelectronic tunneling devices.

4 Methods

Raman and photoluminescence (PL, SPEX/403) spectra exciting by 532 nm laser were measured at room temperature (300 K) and low temperature (200 K and 100 K). The transmission spectra of 1L-hBN were obtained using a spectrophotometer (Jinghua UV1901) with the wavelength in the range of 200 to 1,100 nm. Using the same equipment, the transmission spectra of WS_2/MoS_2 and WS_2/hBN/MoS_2 vdWHs from 360 to 1,100 nm were measured. The optical properties of the three samples were explored by SE (J. A. Woollam, Inc. M2000X-FB-300XTF) at room temperature over a photon energy range from 1.2 to 6.5 eV (513 data points). And the ellipsometric data (ψ, Δ) were collected at fixed incident angle of 65 degree, but the samples were rotated during SE measurement for verifying their in-plane isotropy.

Acknowledgments

The work was financially supported by the National Natural Science Foundation of China (Nos. 11674062, 61775042, and 61774040), the Fudan University–CIOMP Joint Fund (Nos. FC2019-004, FC2019-006, and FC2018-002), the National Key R&D Program of China (No. 2018YFA0703700), the Shanghai Municipal Science and Technology Commission (No. 18JC1410300) and the Shanghai Municipal Natural Science Foundation (No. 20ZR1403200).

Electronic Supplementary Material: Supplementary material (Raman spectrum of 1L-hBN sample at room temperature with a 532 nm excitation. PL spectra of the WS_2/MoS_2 and WS_2/hBN/MoS_2 films excited with a 532 nm laser at different temperature (100, 200, and 300 K) and locations (5 random locations over the whole film surface). The location dependent PL spectra declare the uniform of the vdWHs. Analysis details of spectroscopic ellipsometry measurement. Entire fitting parameters of CPs and excitons in WS_2/MoS_2 and WS_2/hBN/MoS_2 vdWHs) is available in the online version of this article at https://doi.org/10.1007/s12274-021-3774-4.

References

[1] Zhou, X.; Hu, X. Z.; Yu, J.; Liu, S. Y.; Shu, Z. W.; Zhang, Q.; Li, H. Q.; Ma, Y.; Xu, H.; Zhai, T. Y. 2D layered material-based van der Waals heterostructures for optoelectronics. *Adv. Funct. Mater.* **2018**, *28*, 1706587.

[2] Shim, J.; Kang, D. H.; Kim, Y.; Kum, H.; Kong, W.; Bae, S. H.; Almansouri, I.; Lee, K.; Park, J. H.; Kim, J. Recent progress in van der Waals (vdW) heterojunction-based electronic and optoelectronic devices. *Carbon* **2018**, *133*, 78–89.

[3] Zhu, S.; Gong, L. J.; Xie, J. N.; Gu, Z. J.; Zhao, Y. L. Design, synthesis, and surface modification of materials based on transition-metal dichalcogenides for biomedical applications. *Small Methods* **2017**, *1*, 1700220.

[4] Hu, W.; Yang, J. L. Two-dimensional van der Waals heterojunctions for functional materials and devices. *J. Mater. Chem. C* **2017**, *5*, 12289–12297.

[5] Gupta, A.; Sakthivel, T.; Seal, S. Recent development in 2D materials beyond graphene. *Prog. Mater. Sci.* **2015**, *73*, 44–126.

[6] Singh, E.; Kim, K. S.; Yeom, G. Y.; Nalwa, H. S. Atomically thin-layered molybdenum disulfide (MoS_2) for bulk-heterojunction solar cells. *ACS Appl. Mater. Interfaces* **2017**, *9*, 3223–3245.

[7] Cheng, R.; Li, D. H; Zhou, H. L.; Wang, C.; Yin, A. X.; Jiang, S.; Liu, Y.; Chen, Y.; Huang, Y.; Duan, X. F. Electroluminescence and photocurrent generation from atomically sharp WSe_2/MoS_2 heterojunction p-n diodes. *Nano Lett.* **2014**, *14*, 5590–5597.

[8] Ross, J. S.; Rivera, P.; Schaibley, J.; Lee-Wong, E.; Yu, H. Y.; Taniguchi, T.; Watanabe, K.; Yan, J. Q.; Mandrus, D.; Cobden, D. et al. Interlayer exciton optoelectronics in a 2D heterostructure p-n junction. *Nano Lett.* **2017**, *17*, 638–643.

[9] Sundaram, R. S.; Engel, M.; Lombardo, A.; Krupke, R.; Ferrari, A. C.; Avouris, P.; Steiner, M. Electroluminescence in single layer MoS_2. *Nano Lett.* **2013**, *13*, 1416–1421.

[10] Zhang, W. J.; Huang, J. K.; Chen, C. H.; Chang, Y. H.; Cheng, Y. J.; Li, L. J. High-gain phototransistors based on a CVD MoS_2 monolayer. *Adv. Mater.* **2013**, *25*, 3456–3461.

[11] Zheng, Y.; Xiang, D.; Zhang, J. L.; Guo, R.; Wang, W. H.; Liu, T.; Loh, L. Y.; Wang, Y. N.; Gao, J.; Han, C. et al. Controlling phase transition in WSe_2 towards ideal n-type transistor. *Nano Res.* **2021**, *14*, 2703–2710.

[12] Dalila, R. N.; Md Arshad, M. K.; Gopinath, S. C. B.; Norhaimi, W. M. W.; Fathil, M. F. M. Current and future envision on developing biosensors aided by 2D molybdenum disulfide (MoS_2) productions. *Biosens. Bioelectron.* **2019**, *132*, 248–264.

[13] Choi, J. M.; Jang, H. Y.; Kim, A. R.; Kwon, J. D.; Cho, B.; Park, M. H.; Kim, Y. H. Ultra-flexible and rollable 2D-MoS_2/Si heterojunction-based near-infrared photodetector via direct synthesis. *Nanoscale* **2021**, *13*, 672–680.

[14] Li, J. Y.; Ding, Y.; Zhang, D. W.; Zhou, P. Photodetectors based on two-dimensional materials and their van der waals heterostructures. *Acta Phys. Chim. Sin.* **2019**, *35*, 1058–1077.

[15] Wasalathilake, K. C.; Hu, N.; Fu, S. Y.; Zheng, J. C.; Du, A. J.; Yan, C. High capacity and mobility in germanium sulfide/graphene

(GeS/Gr) van der Waals heterostructure as anode materials for sodium–ion batteries: A first-principles investigation. *Appl. Surf. Sci.* **2021**, *536*, 147779.

[16] Pataniya, P. M.; Late, D.; Sumesh, C. K. Photosensitive WS_2/ZnO nano-heterostructure-based electrocatalysts for hydrogen evolution reaction. *ACS Appl. Energy Mater.* **2021**, *4*, 755–762.

[17] Lin, Y.; Pan, D. M.; Luo, H. Hollow direct Z–scheme CdS/$BiVO_4$ composite with boosted photocatalytic performance for RhB degradation and hydrogen production. *Mater. Sci. Semicond. Process.* **2021**, *121*, 105453.

[18] Li, X.; Zhang, S.; Wang, X. J.; Huang, G. F.; Xia, L. X.; Hu, W. Y.; Huang, W. Q. A two-dimensional MoS_2/SnS heterostructure for promising photocatalytic performance: First-principles investigations. *Phys. E Low Dimens. Syst. Nanostruct.* **2021**, *126*, 114453.

[19] Novoselov, K. S.; Geim, A. K.; Morozov, S. V.; Jiang, D.; Zhang, Y.; Dubonos, S. V.; Grigorieva, I. V.; Firsov, A. A. Electric field effect in atomically thin carbon films. *Science* **2004**, *306*, 666–669.

[20] Withers, F.; Del Pozo-Zamudio, O.; Mishchenko, A.; Rooney, A. P.; Gholinia, A.; Watanabe, K.; Taniguchi, T.; Haigh, S. J.; Geim, A. K.; Tartakovskii, A. I. et al. Light-emitting diodes by band-structure engineering in van der Waals heterostructures. *Nat. Mater.* **2015**, *14*, 301–306.

[21] Fang, H.; Battaglia, C.; Carraro, C.; Nemsak, S.; Ozdol, B.; Kang, J. S.; Bechtel, H. A.; Desai, S. B.; Kronast, F.; Unal, A. A. et al. Strong interlayer coupling in van der Waals heterostructures built from single-layer chalcogenides. *Proc. Natl. Acad. Sci. USA* **2014**, *111*, 6198–6202.

[22] Binder, J.; Withers, F.; Molas, M. R.; Faugeras, C.; Nogajewski, K.; Watanabe, K.; Taniguchi, T.; Kozikov, A.; Geim, A. K.; Novoselov, K. S. et al. Sub-bandgap voltage electroluminescence and magneto-oscillations in a WSe_2 light-emitting van der Waals heterostructure. *Nano Lett.* **2017**, *17*, 1425–1430.

[23] Geim, A. K.; Grigorieva, I. V. Van der Waals heterostructures. *Nature* **2013**, *499*, 419–425.

[24] Chiu, M. H.; Li, Y. M.; Zhang, W. G.; Hsu, W. T.; Chang, W. H.; Terrones, M.; Terrones, H.; Li, L. J. Spectroscopic signatures for interlayer coupling in MoS_2-WSe_2 van der Waals stacking. *ACS Nano* **2014**, *8*, 9649–9656.

[25] Gao, S. Y.; Yang, L.; Spataru, C. D. Interlayer coupling and gate-tunable excitons in transition metal dichalcogenide heterostructures. *Nano Lett.* **2017**, *17*, 7809–7813.

[26] Xia, W. S.; Dai, L. P.; Yu, P.; Tong, X.; Song, W. P.; Zhang, G. J.; Wang, Z. M. Recent progress in van der Waals heterojunctions. *Nanoscale* **2017**, *9*, 4324–4365.

[27] Pant, A.; Mutlu, Z.; Wickramaratne, D.; Cai, H.; Lake, R. K.; Ozkan, C.; Tongay, S. Fundamentals of lateral and vertical heterojunctions of atomically thin materials. *Nanoscale* **2016**, *8*, 3870–3887.

[28] Torun, E.; Miranda, H. P. C.; Molina-Sánchez, A.; Wirtz, L. Interlayer and intralayer excitons in MoS_2/WS_2 and $MoSe_2$/WSe_2 heterobilayers. *Phys. Rev. B* **2018**, *97*, 245427.

[29] Zhu, X. D.; He, J. B.; Zhang, R. J.; Cong, C. X.; Zheng, Y. X.; Zhang, H.; Zhang, S. W.; Chen, L. Y. Effects of dielectric screening on the excitonic and critical points properties of WS_2/MoS_2 heterostructures. *Nanoscale* **2020**, *12*, 23732–23739.

[30] Chernikov, A.; Berkelbach, T. C.; Hill, H. M.; Rigosi, A.; Li, Y. L.; Aslan, O. B.; Reichman, D. R.; Hybertsen, M. S.; Heinz, T. F. Exciton binding energy and nonhydrogenic Rydberg series in monolayer WS_2. *Phys. Rev. Lett.* **2014**, *113*, 076802.

[31] Latini, S.; Winther, K. T.; Olsen, T.; Thygesen, K. S. Interlayer excitons and band alignment in MoS_2/hBN/WSe_2 van der Waals heterostructures. *Nano Lett.* **2017**, *17*, 938–945.

[32] Nayak, P. K.; Horbatenko, Y.; Ahn, S.; Kim, G.; Lee, J. U.; Ma, K. Y.; Jang, A. R.; Lim, H.; Kim, D.; Ryu, S. et al. Probing evolution of twist-angle-dependent interlayer excitons in $MoSe_2$/WSe_2 van der Waals heterostructures. *ACS Nano* **2017**, *11*, 4041–4050.

[33] Wilson, N. R.; Nguyen, P. V.; Seyler, K.; Rivera, P.; Marsden, A. J.; Laker, Z. P. L.; Constantinescu, G. C.; Kandyba, V.; Barinov, A.; Hine, N. D. M. et al. Determination of band offsets, hybridization, and exciton binding in 2D semiconductor heterostructures. *Sci. Adv.* **2017**, *3*, e1601832.

[34] Bradley, A. J.; Ugeda, M. M.; Da Jornada, F. H.; Qiu, D. Y.; Ruan, W.; Zhang, Y.; Wickenburg, S.; Riss, A.; Lu, J.; Mo, S. K. et al. Probing the role of interlayer coupling and coulomb interactions on electronic structure in few-layer $MoSe_2$ nanostructures. *Nano Lett.* **2015**, *15*, 2594–2599.

[35] Wang, G.; Chernikov, A.; Glazov, M. M.; Heinz, T. F.; Marie, X.; Amand, T.; Urbaszek, B. Excitons in atomically thin transition-metal dichalcogenides. *Rev. Mod. Phys.* **2018**, *90*, 021001.

[36] Zhu, X. D.; Zhang, R. J.; Zheng, Y. X.; Wang, S. Y.; Chen, L. R. Spectroscopic ellipsometry and its applications in the study of thin film materials. *Chin. Opt.* **2019**, *12*, 1195.

[37] Shi, Y. J.; Zhang, R. J.; Zheng, H.; Li, D. H.; Wei, W.; Chen, X.; Sun, Y.; Wei, Y. F.; Lu, H. L.; Dai, N. et al. Optical constants and band gap evolution with phase transition in sub-20-nm-thick TiO_2 films prepared by ALD. *Nanoscale Res. Lett.* **2017**, *12*, 243.

[38] He, J. B.; Jiang, W.; Zhu, X. D.; Zhang, R. J.; Wang, J. L.; Zhu, M. P.; Wang, S. Y.; Zheng, Y. X.; Chen, L. Y. Optical properties of thickness-controlled $PtSe_2$ thin films studied via spectroscopic ellipsometry. *Phys. Chem. Chem. Phys.* **2020**, *22*, 26383–26389.

[39] Zhu, X. D.; Li, D. H.; Zhang, R. J.; Zhang, H.; Cong, C. X.; Zhu, M. P.; Shi, Y. J.; Wu, Y.; Wang, S. Y.; Zheng, Y. X. et al. Probing quantum confinement effects on the excitonic property and electronic band structures of MoS_2. *Appl. Surf. Sci.* **2020**, *519*, 146262.

[40] Shen, W. F.; Wei, Y. X.; Hu, C. G.; López-Posadas, C. B.; Hohage, M.; Sun, L. D. Substrate induced optical anisotropy in monolayer MoS_2. *J. Phys. Chem. C* **2020**, *124*, 15468–15473.

[41] Yang, J. Y.; Zhang, W. J.; Liu, L. H. Anisotropic dielectric functions of (0001) sapphire from spectroscopic ellipsometry and first-principles study. *Phys. B:Condens. Matter* **2015**, *473*, 35–41.

[42] Li, D. H.; Zheng, H.; Wang, Z. Y.; Zhang, R. J.; Zhang, H.; Zheng, Y. X.; Wang, S. Y.; Zhang, D. W.; Chen, L. Y. Dielectric functions and critical points of crystalline WS_2 ultrathin films with tunable thickness. *Phys. Chem. Chem. Phys.* **2017**, *19*, 12022–12031.

[43] Vu, Q. A.; Lee, J. H.; Nguyen, V. L.; Shin, Y. S.; Lim, S. C.; Lee, K.; Heo, J.; Park, S.; Kim, K.; Lee, Y. H. et al. Tuning carrier tunneling in van der Waals heterostructures for ultrahigh detectivity. *Nano Lett.* **2017**, *17*, 453–459.

[44] Zhang, X.; Han, W. P.; Wu, J. B.; Milana, S.; Lu, Y.; Li, Q. Q.; Ferrari, A. C.; Tan, P. H. Raman spectroscopy of shear and layer breathing modes in multilayer MoS_2. *Phys. Rev. B* **2013**, *87*, 115413.

[45] Peimyoo, N.; Shang, J. Z.; Yang, W. H.; Wang, Y. L.; Cong, C. X.; Yu, T. Thermal conductivity determination of suspended mono- and bilayer WS_2 by Raman spectroscopy. *Nano Res.* **2015**, *8*, 1210–1221.

[46] Liang, L. B.; Meunier, V. First-principles Raman spectra of MoS_2, WS_2 and their heterostructures. *Nanoscale* **2014**, *6*, 5394–5401.

[47] Mouri, S.; Zhang, W. J.; Kozawa, D.; Miyauchi, Y.; Eda, G.; Matsuda, K. Thermal dissociation of inter-layer excitons in MoS_2/$MoSe_2$ hetero-bilayers. *Nanoscale* **2017**, *9*, 6674–6679.

[48] Tran, M. D.; Kim, J. H.; Lee, Y. H. Tailoring photoluminescence of monolayer transition metal dichalcogenides. *Curr. Appl. Phys.* **2016**, *16*, 1159–1174.

[49] Grundmann, M., *The Physics of Semiconductors*; Springer: Berlin Heidelberg, 2006; pp 232–235.

[50] Cong, C. X.; Shang, J. Z.; Wang, Y. L.; Yu, T. Optical properties of 2D semiconductor WS_2. *Adv. Opt. Mater.* **2018**, *6*, 1700767.

[51] Deilmann, T.; Thygesen, K. S. Interlayer trions in the MoS_2/WS_2 van der Waals heterostructure. *Nano Lett.* **2018**, *18*, 1460–1465.

[52] Yu, Y. F.; Hu, S.; Su, L. Q.; Huang, L. J.; Liu, Y.; Jin, Z. H.; Purezky, A. A.; Geohegan, D. B.; Kim, K. W.; Zhang, Y. et al. Equally efficient interlayer exciton relaxation and improved absorption in epitaxial and nonepitaxial MoS_2/WS_2 heterostructures. *Nano Lett.* **2015**, *15*, 486–491.

[53] Heo, H.; Sung, J. H.; Cha, S.; Jang, B. G.; Kim, J. Y.; Jin, G.; Lee, D.; Ahn, J. H.; Lee, M. J.; Shim, J. H. et al. Interlayer orientation-dependent light absorption and emission in monolayer semiconductor stacks. *Nat. Commun.* **2015**, *6*, 7372.

[54] Shang, J. Z.; Shen, X. N.; Cong, C. X.; Peimyoo, N.; Cao, B. C.;

Eginligil, M.; Yu, T. Observation of excitonic fine structure in a 2D transition-metal dichalcogenide semiconductor. *ACS Nano* **2015**, *9*, 647–655.

[55] Peimyoo, N.; Yang, W. H.; Shang, J. Z.; Shen, X. N.; Wang, Y. L.; Yu, T. Chemically driven tunable light emission of charged and neutral excitons in monolayer WS_2. *ACS Nano* **2014**, *8*, 11320–11329.

[56] Lin, Y. X.; Ling, X.; Yu, L. L.; Huang, S. X.; Hsu, A. L.; Lee, Y. H.; Kong, J.; Dresselhaus, M. S.; Palacios, T. Dielectric screening of excitons and trions in single-layer MoS_2. *Nano Lett.* **2014**, *14*, 5569–5576.

[57] Li, L. H.; Santos, E. J. G.; Xing, T.; Cappelluti, E.; Roldán, R.; Chen, Y.; Watanabe, K.; Taniguchi, T. Dielectric screening in atomically thin boron nitride nanosheets. *Nano Lett.* **2015**, *15*, 218–223.

[58] Latini, S.; Olsen, T.; Thygesen, K. S. Excitons in van der Waals heterostructures: The important role of dielectric screening. *Phys. Rev. B* **2015**, *92*, 245123.

[59] Koo, J.; Gao, S. Y.; Lee, H.; Yang, L. Vertical dielectric screening of few-layer van der Waals semiconductors. *Nanoscale* **2017**, *9*, 14540–14547.

[60] Fujiwara, H., *Spectroscopic Ellipsometry*: *Principles and Applications*; John Wiley & Sons: New York, 2007.

[61] Li, W.; Birdwell, A. G.; Amani, M.; Burke, R. A.; Ling, X.; Lee, Y. H.; Liang, X. L.; Peng, L. M.; Richter, C. A.; Kong, J. et al. Broadband optical properties of large-area monolayer CVD molybdenum disulfide. *Phys. Rev. B* **2014**, *90*, 195434.

[62] Yu, P. Y.; Cardona, M., *Fundamentals of Semiconductors*: *Physics and Materials Properties*; 4th ed. Springer: Heidelberg, 2010; pp 788.

[63] Le, N. B.; Huan, T. D.; Woods, L. M. Interlayer interactions in van der Waals heterostructures: Electron and phonon properties. *ACS Appl. Mater. Interfaces* **2016**, *8*, 6286–6292.

[64] Wu, M. H.; Qian, X. F.; Li, J. Tunable exciton funnel using moiré superlattice in twisted van der Waals bilayer. *Nano Lett.* **2014**, *14*, 5350–5357.

[65] Shi, J.; Li, Y. Z.; Zhang, Z. P.; Feng, W. Q.; Wang, Q.; Ren, S. L.; Zhang, J.; Du, W. N.; Wu, X. X.; Sui, X. Y. et al. Twisted-angle-dependent optical behaviors of intralayer excitons and trions in WS_2/WSe_2 heterostructure. *ACS Photonics* **2019**, *6*, 3082–3091.

[66] Sharma, A.; Harnish, P.; Sylvester, A.; Kotov, V. N.; Neto, A. H. C. Van der Waals forces and electron-electron interactions in two strained graphene layers. *Phys. Rev. B* **2014**, *89*, 235425.

[67] Li, D. H.; Song, X. F.; Xu, J. P.; Wang, Z. Y.; Zhang, R. J.; Zhou, P.; Zhang, H.; Huang, R. Z.; Wang, S. Y.; Zheng, Y. X. et al. Optical properties of thickness-controlled MoS_2 thin films studied by spectroscopic ellipsometry. *Appl. Surf. Sci.* **2017**, *421*, 884–890.

[68] Waldecker, L.; Raja, A.; Rösner, M.; Steinke, C.; Bostwick, A.; Koch, R. J.; Jozwiak, C.; Taniguchi, T.; Watanabe, K.; Rotenberg, E. et al. Rigid band shifts in two-dimensional semiconductors through external dielectric screening. *Phys. Rev. Lett.* **2019**, *123*, 206403.